Chapter 2

Post-Reionization H I power spectrum and detection challenges

21 cm signal from the spin-flip transition of electrons in neutral hydrogen is an efficient way to probe various ages of the universe. We are mainly working here in the post-reionization era of the universe which is an era of galaxy formation and evolution. Being too faint, we can't observe the 21 cm signal directly. Bharadwaj and Ali (2005) discuss the evolution of neutral hydrogen in the Dark Ages, pre reionization era, the reionization era and the post-reionization era. Sarkar and Bharadwaj (2019); Sarkar et al. (2016) modify it by modifying the bias function and including the effect of redshift space distortion. In this chapter, we will discuss the model of the 21 cm power spectrum in the post-reionization era.

2.1 Dark Matter power spectrum

The matter power spectrum in the universe explains the local density fluctuation with respect to its mean. Let $\rho(\vec{x})$ represent the matter density at a particular point in the

universe and $\bar{\rho}$ represent the mean density of the universe, then the fluctuation in the matter density can be written as

$$\delta(\vec{x}) = \frac{\rho(\vec{x}) - \bar{\rho}}{\bar{\rho}}, \tag{2.1}$$

here $\delta(\vec{x})$ is a dimensionless quantity that represents the density fluctuation of the universe. Fourier modes of $\delta(\vec{x})$ are defined as

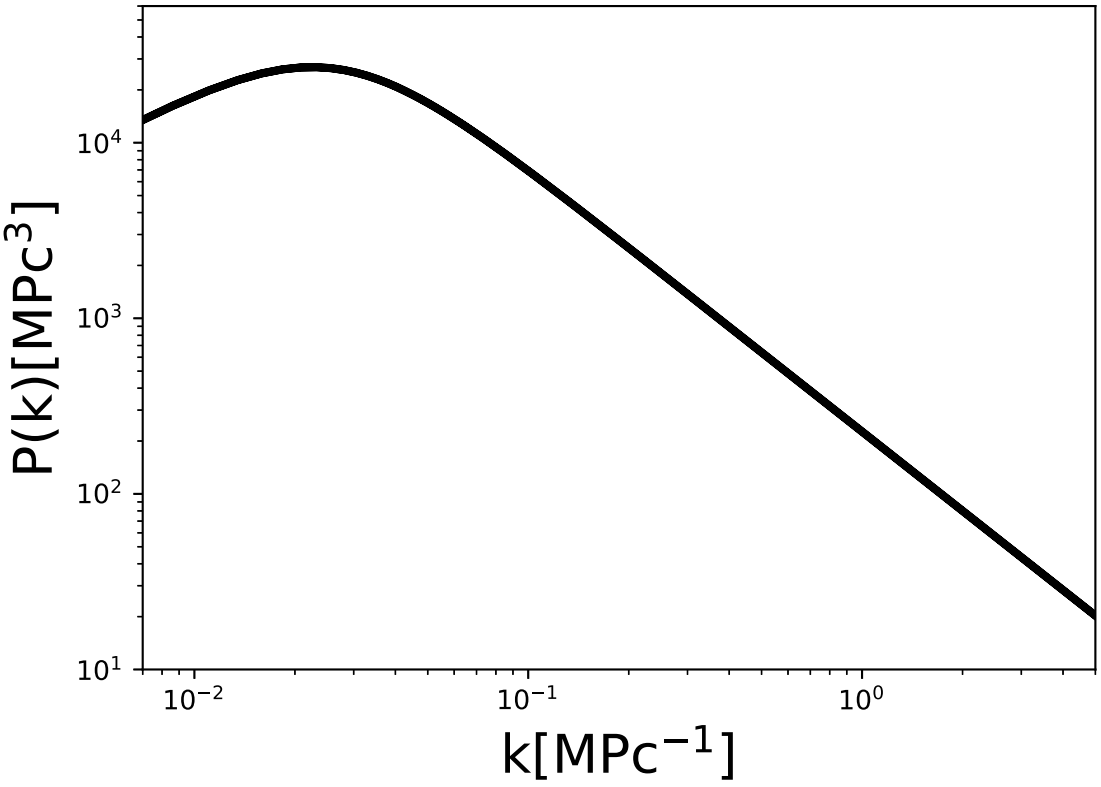

Figure 2.1: Dark matter power spectrum in units of MPc^3 as a function of wavevector

$$\Delta(\vec{k}) = \int d\vec{x} e^{i\vec{k}.\vec{x}} \delta(\vec{x}) \tag{2.2}$$

The isotropic dark matter power spectrum is denoted as P(k) and has a dimension of $(length)^3$. A parametric form of the DM power spectrum is taken from (Peacock and

Dodds, 1994)

$$P(k) = \frac{2\pi^2}{k^3}\Delta^2(k) \tag{2.3}$$

where $\Delta^2(k)$ is given as

$\Delta^2(k) = \frac{(k/k_0)^\alpha}{1+(k/k_C)^{\alpha-\beta}}$

$k_0 = 0.29 \pm 0.01\ h$ Mpc $^{-1}$

$k_1 = 0.039 \pm 0.002\ h$ Mpc $^{-1}$

$\alpha = 1.50 \pm 0.03$

$\beta = 4.0 \pm 0.5$

It is known that in ΛCDM cosmology, the angular diameter distance to any object at a redshift z increases to a redshift of ~ 1.5 and shows a slow decrease with redshift afterwards. The luminosity distance to an object, on the other hand, increases monotonically with redshift. This makes any high redshift object appear increasingly smaller in angular size with decreasing flux as the redshift changes up to a redshift of 1.5. For astrophysical objects at higher redshifts, the flux decreases continuously, however, the angular size shows a slight increase with redshift. We choose three redshifts for this study, redshifts of $1.25, 1.5$ and 3.0, to scan the effects of the above change in the power spectrum.

2.2 H I power spectrum

At radio wavelengths, we observe the brightness temperature fluctuations. The 21 cm brightness temperature fluctuation from a direction $\hat{n}$ and redshift z is given as

$$\delta T_b(\vec{n}, z) = \frac{(T_s - T_\gamma)\tau}{1+z} \tag{2.4}$$

where T_s is the spin temperature, T_γ is the CMBR temperature and τ is the 21 cm optical depth. This equation is valid for low optical depth. We can also write the brightness

temperature as

$$\delta T_b = \bar{T}(z)\,\eta_{HI}(\vec{n},z) \tag{2.5}$$

where $\bar{T}(z)$ depends on redshift and cosmological background

$$\bar{T}(z) = 4.0mK(1+z)^2\left(\frac{\Omega_b h^2}{0.02}\right)\left(\frac{0.7}{h}\right)\frac{H_0}{H(z)} \tag{2.6}$$

and $\eta_{HI}(\vec{n},z)$ is called "21 cm radiation efficiency" which can be written as

$$\eta(\vec{n},z) = \frac{\rho_{HI}}{\bar{\rho}_H}\left(1-\frac{T_\gamma}{T_s}\right)\left[1-\frac{1+z}{H(z)}\frac{\partial v}{\partial r}\right]. \tag{2.7}$$

"21 cm radiation efficiency" varies with redshift by the mean neutral hydrogen density in the universe and also it depends upon peculiar velocity whose effect is included in the last term. "21 cm radiation efficiency" in the Fourier space can be written as

$$\eta(\vec{n},z) = \int \frac{d^3k}{(2\pi)^3} e^{-i\vec{k}.\vec{x}}\tilde{\eta}_{HI}(\vec{k},z) \tag{2.8}$$

where $\vec{x} = r_v\hat{n}$ is a comoving position vector in the plane of the sky.

We define the H I power spectrum at any redshift using "21 cm radiation efficiency" as

$$< \eta^*_{HI}(\vec{k})\,\eta_{HI}(\vec{k'}) >= (2\pi)^3\delta_{3D}(\vec{k}-\vec{k'})P_{HI}(\vec{k},z). \tag{2.9}$$

where $P_{HI}(\vec{k},z)$ is the H I power spectrum and δ_{3D} is the three-dimensional Dirac delta function.

2.2.1 Modelling redshifted 21 cm power spectrum

Model for the H I power spectrum in the post reionization era is discussed in Bharadwaj and Ali (2005), where they used the dark matter power spectrum and a scale independent

bias to model the H I signal. Better models for the signal are presented is Sarkar and Bharadwaj (2018); Sarkar et al. (2016), where they used numerical simulation to calculate the effect of scale dependent bias as well as redshift space distortion factor. The H I power spectrum can be written as

$$P_{HI}(\vec{k_\perp}, k_\parallel) = b(k)^2 \left[1 + 2r\beta\mu^2 + \beta^2\mu^4\right] D_{FoG}(k_\parallel, \sigma_p) P(k), \tag{2.10}$$

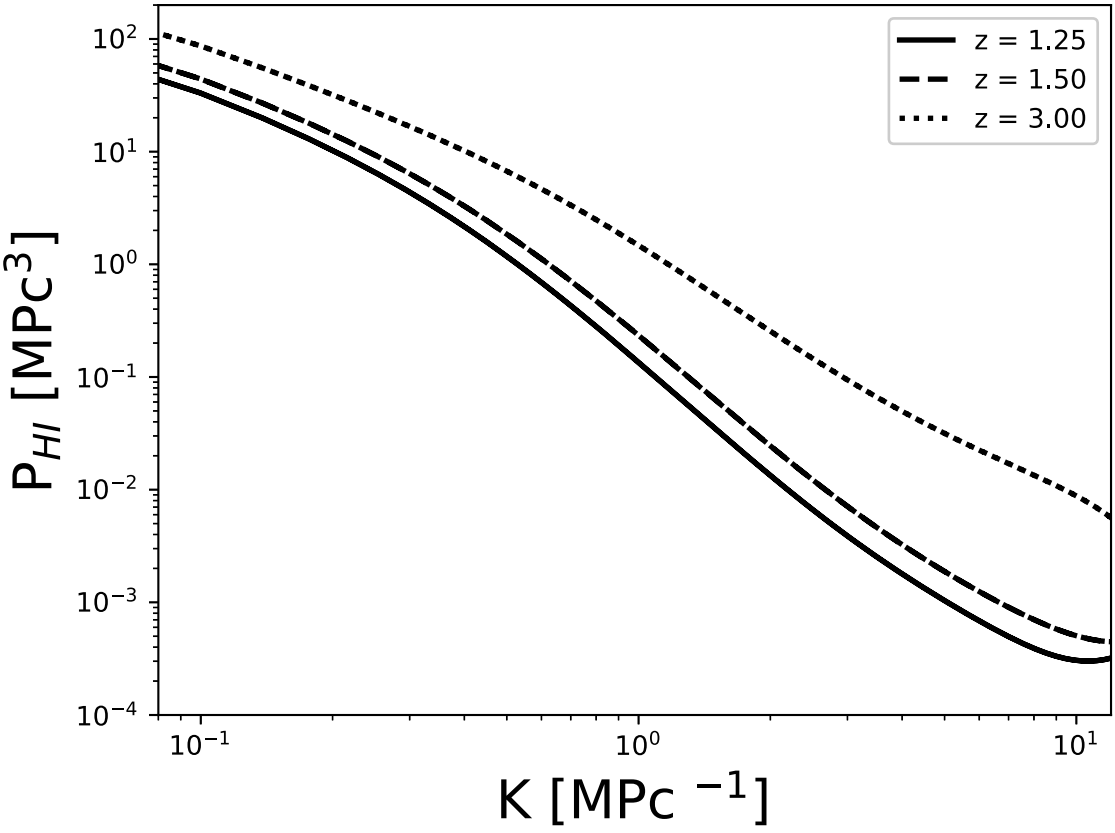

Figure 2.2: H I power spectrum with GMRT as a function of wavevector for three post-reionization redshifts

where $b(k)$ is the scale dependent bias defined as $b(k) = \sqrt{\frac{P_{HI}(k)}{P(k)}}$ in the absence of redshift space distortion. σ_p is a parameter for the redshifted space distortion. Both of these depend on the redshift and wave number. The factor $\mu = k_\parallel/k$. The H I power spectrum for post-reionization redshifts is shown in the Fig 2.2

2.2.2 21 cm Angular power spectrum

Let $\delta I(\vec{\theta}, z_s)$ be the specific intensity fluctuation of H I emission originated at the redshift z_s from a direction $\vec{\theta}$ in the sky with respect to the centre of the field of view of observation $\vec{n_0}$ i.e. $\vec{\theta} = \hat{n} - \hat{n}_0$. We define $\Delta\tilde{I}(\vec{U})$ as the Fourier transform of $\delta\tilde{I}(\vec{\theta}, z_s)$

$$\Delta\tilde{I}(\vec{U}, z_s) = \int d\vec{\theta}\, \delta I(\vec{\theta}, z_s) e^{-i2\pi\vec{U}.\vec{\theta}}. \tag{2.11}$$

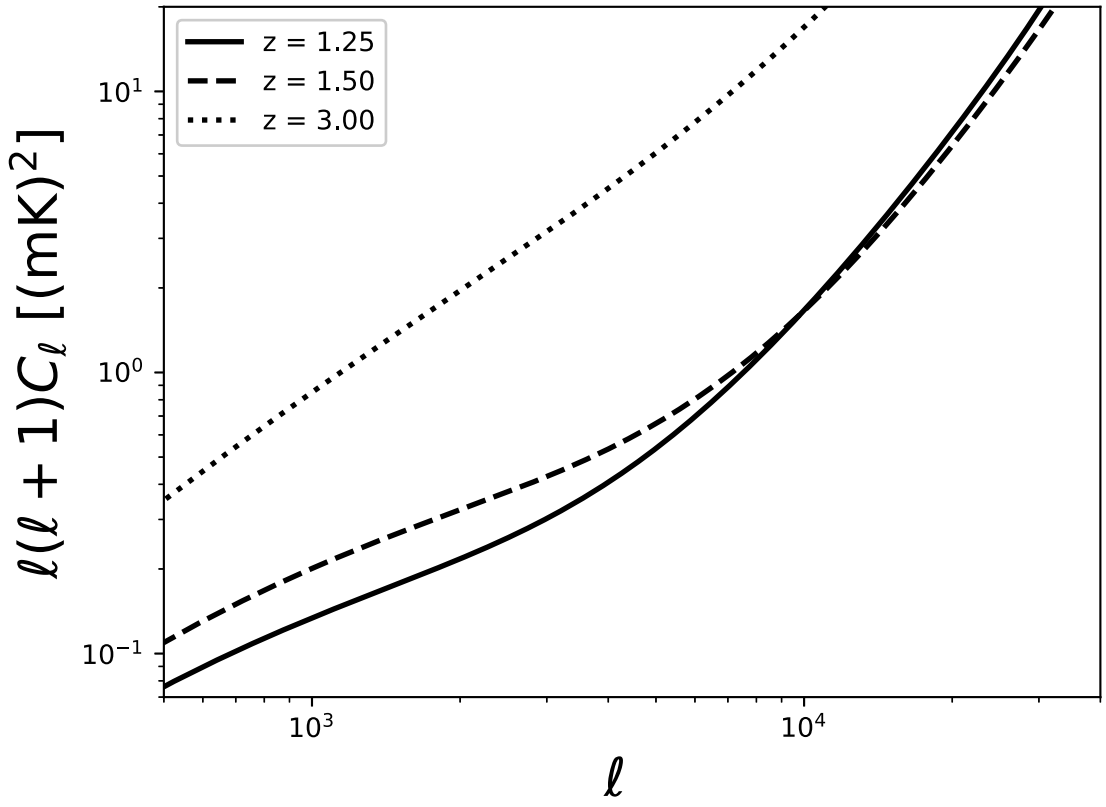

Figure 2.3: Figure shows 21 cm angular power spectra for redshifts of 1.25, 1.5, 3.0 using the models from Ade et al. and Collaboration (2016); Bharadwaj and Ali (2005); Sarkar and Bharadwaj (2018); Sarkar et al. (2016) as described in the text.

The vector $\vec{U}$, we refer as 'baseline', is the Fourier conjugate to the vector $\vec{\theta}$. Assuming the specific intensity fluctuations to be statistically isotropic, angular power spectrum C_l of

redshift	z=1.25	z= 1.5	z=2.5
θ_0 ($'$)	22	24	39
U_M [kλ]	52.6	47.3	29.6

Table 2.1: The parameters θ_0 and maximum baselines for observations of redshifted 21 cm emission from redshifts 1.25, 1.5 and 3 for the uGMRT.

the 21 cm brightness fluctuations at a multipole $l = 2\pi U$, ($U = \mid \vec{U} \mid$) can be written as

$$\langle \Delta\tilde{I}(\vec{U}, z_s)\Delta\tilde{I}^*(\vec{U}, z_s)\rangle = \delta_{2D}(\vec{U} - \vec{U}') \left(\frac{\partial B}{\partial T}\right)^2 C_l. \tag{2.12}$$

Here we use angular brackets $<>$ to represent the ensemble average and δ_{2D} is the two dimensional Dirac delta function. The angular power spectrum C_l probes the matter power spectrum at the source redshift z_s (see for example Choudhuri et al. (2014)).The angular power spectrum of H I is shown in the Fig 2.3 at three different sources redshift 1.25, 1.5 and 3. 21 cm angular spectrum and dark matter power spectrum are related as

$$C_{l_g} = \left(\frac{\partial B}{\partial T}\right)^{-2} b(k)^2 \left[1 + 2r\beta\mu^2 + \beta^2\mu^4\right] D_{FoG}(k_{\parallel}, \sigma_p) P(k), \tag{2.13}$$

For the observational purpose, we consider the parameters and baseline of the uGMRT* (Gupta et al., 2017). The uGMRT has an aperture diameter of 45 meters with the largest antenna separation of 25 km. For simplicity, here we assume a Gaussian aperture for the antenna and list the values of the parameter θ_0 corresponding to the three redshifts in Table 2.1. The maximum antenna separation for the uGMRT is 25 km. Since the angular multipole $l = 2\,\pi\,U$, the range of multipoles at which the uGMRT is sensitive to are $\sim 310 - 330,000$, $\sim 280 - 300,000$, $\sim 180 - 187,000$ for the redshifts $1.25, 1.5$ and 3.0 respectively.

*uGMRT: upgraded Giant Meterwave Radio Telescope

2.3 Radio interferometer as a probe of 21 cm power spectrum

Radio interferometer measures the visibility signal which is the Fourier transformation of sky brightness distribution. Each pair of antennae in a radio interferometer corresponds to one baseline vector at a time. Further, they measure the visibility only at points where baselines are present i.e. the measurement depends upon the antenna distributions. The visibility function is a continuous complex function and can be written as

$$V(\vec{U},\nu) = \int d^2\theta A(\vec{\theta})\delta I_\nu(\vec{\theta},z_s)e^{-i2\pi\vec{U}.\vec{\theta}} \tag{2.14}$$

where $V(\vec{U},\nu)$ is the visibility signal, $I_\nu(\vec{\theta})$ is the specific intensity distribution and $A(\vec{\theta})$ is the telescope's primary beam pattern, the real component of visibility correlation at the nearby baseline has the information of the redshifted 21 cm power spectrum.

$$V_2(\vec{U},\vec{U'},\nu,\Delta\nu) = \frac{\bar{I}_\nu^2\theta_0^2}{2r_\nu^2}\int_0^\infty dk_\parallel P_{HI}(\nu_\parallel,\vec{k}_\perp)\cos(k_\parallel r'_\nu\Delta\nu). \tag{2.15}$$

where $\bar{I}_\nu$ is the sky intensity and can be written as

$$\bar{I}_\nu = 2.5\times10^2\frac{Jy}{sr}\left(\frac{\Omega_b h^2}{0.02}\right)\left(\frac{0.7}{h}\right)\frac{H_0}{H(z)} \tag{2.16}$$

where θ_0 is the resolution of single telescope dish and r_ν is the comoving distance.

2.4 Effect of foreground

Foreground signal contains Galactic synchrotron emission, free-free emission from ionizing halos, and synchrotron emission from low redshift radio galaxy clusters, which acts as a contamination in the 21 cm signal. There are two kinds of foregrounds that generate major

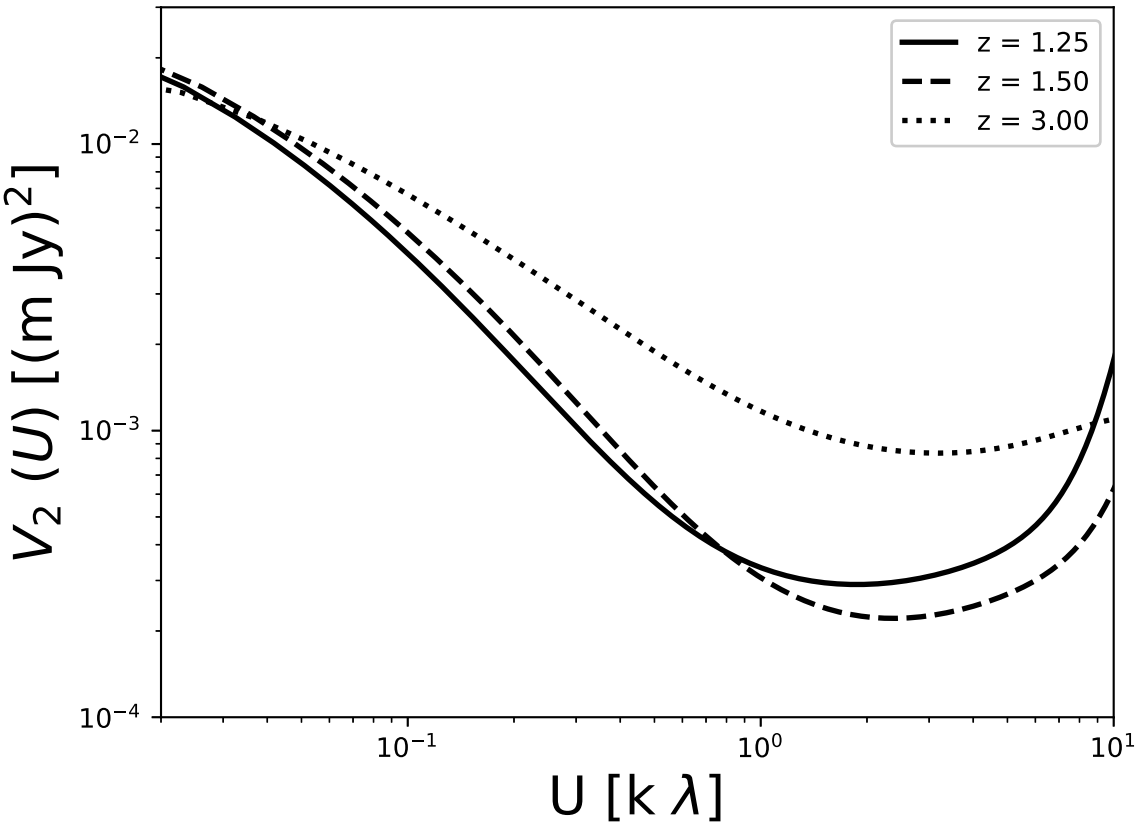

Figure 2.4: Expected visibility correlation with the GMRT as a function of baselines for three post reionization redshifts.

challenges in the observation of a 21 cm signal. One is the Galactic foreground which possesses three parts, First and the largest component is the Diffuse Galactic Synchrotron Emission (DGSE), which is the dominant foreground component. The second component is radio synchrotron emission from discrete sources, mostly supernova remnants (SNRs). The third and last component is the free-free radio emission from diffuse ionized gas, this component has only 1% contribution in the foreground while the other two components are dominating. For the other two parts, we have used the model from Trott (2016) and (Jelić et al., 2008) as

$$< \Delta T_{GS}^2 > (u,\nu) = (\eta T_B)^2 \left(\frac{u}{u_0}\right)^{-2.7} \left(\frac{\nu}{\nu_0}\right)^{-2.55} K^2, \tag{2.17}$$

where $\eta = 0.01$ is the fluctuation level relative to the uniform brightness temperature $T_B = 253$ K, $u_0 = 10$ wavelengths and $\nu_0 = 100$ MHz is the reference frequency. This power law is also shown in Fig 2.5 for three redshifts 1.25, 1.5 and 3. There are two kinds

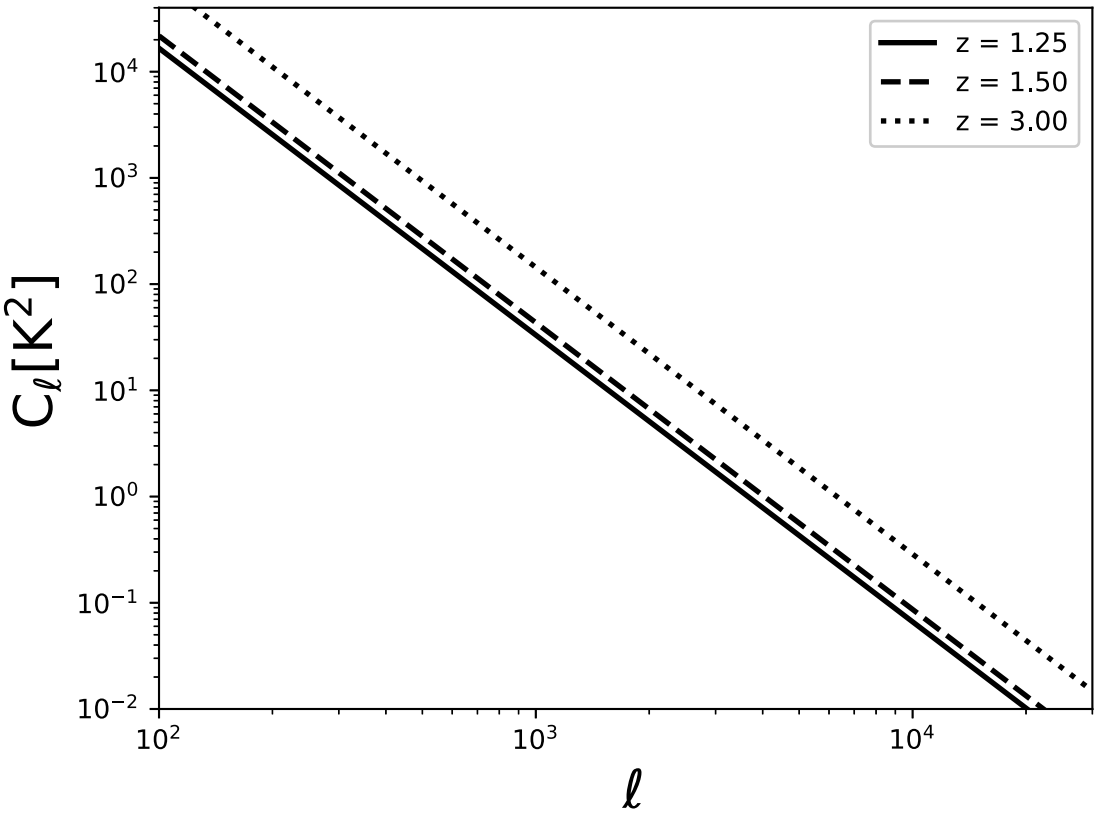

Figure 2.5: Theoretical DGSE power spectrum as a function of multipole for three post-reionization redshifts

of foreground mitigation techniques in order to recover the 21 cm signal. Foreground avoidance involves the removal of that region from observation in which the foreground is present. Second, foreground suppression which involves eliminating the foreground signal by previously modeling it. Several methods for foreground suppression and removal (Cho et al., 2012; Choudhuri et al., 2016; Ghosh et al., 2011) and foreground avoidance (Trott, 2016; Yoshiura et al., 2018) has been discussed. Observationally, there have been

several attempts to quantify the properties of the foreground signal by Chakraborty et al. (2019); Ghosh et al. (2011); Pen et al. (2009). Zhang et al. (2016) use the Bayesian-based semi-blind component separation approach to remove foreground contamination from interferometric observation. Ghosh (2020) uses the Gaussian Process Regression to model both foreground emission and instrumental systematics in ~ 2 hours of observation from the HERA (henceforth HERA[†]).

Another type of foreground source is extragalactic point sources which include the bright radio galaxies whose emission range lies in our frequency emission range. These can be modelled using poisson distribution as discussed in Trott (2016).

2.5 Discussion

Here, we discuss the model of matter, the 21 cm power spectrum and the foreground power spectrum. We concentrate on three redshifts 1.25, 1.5 and 3.0. These models will be used as fiducial cases for our studies henceforth.

- We first describe the mathematical formulation of the 21 cm radiation efficiency, which quantifies the intensity fluctuations of the H I signal. Further H I power spectrum is then introduced, which is defined in terms of the radiation efficiency and the dark matter power spectrum.

- Here we include factors like scale-dependent bias and redshift space distortion in H I power spectrum. We also discuss the angular power spectrum of the H I signal, which is crucial for observational purposes and provides insights into the matter power spectrum at the source redshift.

- Furthermore, we discuss the role of radio interferometers as probes for the 21 cm power spectrum. Visibility signals, obtained through radio interferometry, contain

[†]HERA: Hydrogen Epoch of Reionization Array, South Africa (DeBoer, 2017)

information about the redshifted 21 cm power spectrum and are influenced by primary beam patterns.

- Foreground contamination, including Galactic synchrotron emission and extragalactic point sources, poses significant challenges in detecting the faint H I signal. Various foreground mitigation techniques are discussed, such as foreground avoidance and suppression.